



Contents lists available at ScienceDirect

International Journal of Solids and Structures

journal homepage: www.elsevier.com/locate/ijsolstr

Omnidirectional wave polarization manipulation in isotropic polar solids

Qian Wu, Guoliang Huang*

Department of Mechanical and Aerospace Engineering, University of Missouri, Columbia, MO 65211, USA

ARTICLE INFO

Keywords:

Isotropic polar medium
Stress asymmetry
Chirality
Mode conversion
Anomalous wave polarization

ABSTRACT

Mode conversion and anomalous wave polarization between shear and longitudinal waves have been mainly explored in anisotropic solids. However, the use of elastic anisotropy inevitably introduces fundamental limitation in operative directions, which is not desirable for applications. In this study, we propose to use two-dimensional (2D) isotropic polar media that exhibit polarity and chirality moduli to achieve the above behaviors in an omnidirectional way, thereby realizing omnidirectional wave polarization manipulation. First, we formulate analytically and numerically a nearly perfect wave mode conversion, enabled by the chirality modulus, through a polar slab. Then, we emphasize that the polarity modulus causes the omnidirectional anomalous wave polarization which features faster shear modes. Two supplementary examples of the anomalous wave polarization, including singly polarized transmission and anomalous wave refraction, are presented. The former corresponds to a “fluid-like” or a “shear-wave” solid, depending on the choice of the polarity modulus. While the latter shows a longitudinal incidence causes no shear refraction beyond a critical angle at the interface between a Cauchy and a polar media. All the cases investigated here are directionally independent, drastically differing from those in anisotropic systems. It is our hope that the isotropic polar media could represent a new platform for the exploration of versatile polarization manipulation devices.

0. Introduction

To describe wave propagation in solid media, the particle vibrating direction known as polarization is typically used and is dependent on the material's anisotropy. These polarizations identify the nature of the particle motion with respect to the wave propagation direction (Auld, 1973). In the isotropic elastic solids, elastic waves support both purely longitudinal (P) and shear (S) modes with different phase velocities, where the particle motion is parallel and perpendicular to the wave propagating direction, respectively. How to efficiently manipulate the polarization states of elastic waves has attracted a long-time interest for many potential engineering applications (Park et al., 2020). Among existing wave polarization manipulation approaches, longitudinal-shear mode conversion (Wu et al., 2011; Zhu et al., 2014; Kweun et al., 2017; Noguchi et al., 2015) and anomalous wave polarization (AWP) that supports faster propagation of shear modes (Ledbetter and Kriz, 1982; Schoenberg, 1983; Lee et al., 2017; Ahn et al., 2018; Helbig and Schoenberg, 1987) are two interesting and fundamental topics in anisotropic elastic media. The former enables the energy exchange between longitudinal and shear modes considered generally orthogonal in normal Cauchy solid media. From an application standpoint, studies on mode conversion become increasingly crucial for the efficient shear-wave generators and medical ultrasonic devices (Clement et al., 2004; Tufail et al., 2011; White et al., 2006; Sayers and Tait, 1984). The latter

refers to a polarization transition from longitudinal to shear modes in an anisotropic medium. That said, the shear or quasi-shear modes can outspeed the longitudinal or quasi-longitudinal ones at certain directions. As two examples, longitudinal-wave deceleration (or shear-wave acceleration) and anomalous refraction from the longitudinal incidence into zero transmitted shear components have been found quite useful in wave steering and non-destructive evaluation (Patil et al., 2019). Among all the mentioned works realizing the AWP, Ledbetter and Kriz (1982) first found the faster shear modes with $C_{11} < C_{66}$ in an orthorhombic crystal material. It takes places only along the x -directed material axis. Then, the efforts have been focused on the realization of the AWP along a non-material axis by a transversely isotropic system ($C_{11} = C_{33}$) that exhibits negative Poisson's ratio (Schoenberg, 1983). It was later found that an elastic condition ($C_{\text{off-diagonal}} < -C_{\text{shear}}$, i.e. $C_{13} + C_{44} < 0$) leads to the AWP along non-material axis with negative Poisson's ratio (Helbig and Schoenberg, 1987). On the other hand, a network-based type of isotropic auxetic materials have been attracting increasing attention (Reid et al., 2018, 2019). However, they do not necessarily support the AWP, since the isotropic negative Poisson's ratio does not lead to the crossover between shear and longitudinal modes. To physically realize the AWP, efforts have been mainly focused on the design of elastic metamaterials. Lee et al. (2017) proposed a 2D

* Corresponding author.

E-mail address: huangg@missouri.edu (G. Huang).

non-resonant slit-type metamaterial which exhibits $C_{11} < C_{66} < C_{22}$, regardless of C_{12} , to observe the AWP along the horizontal direction. The designed metamaterials work in the low frequency region, far away from the structural resonance and hence promising broadband operability. Based on their design, mode conversion from longitudinal to shear modes was demonstrated with a metamaterial wedge. Later, the same group utilized topology optimization to design an anisotropic metamaterial ($C_{13} + C_{44} < 0$) to realize the AWP at 45° to the material axis (Ahn et al., 2018). Very recently, a three-dimensional bowtie auxetic lattice, which exhibits a directionally dependent mass density valued from positive to negative, was numerically proposed to exhibit the AWP under the condition $C_{13} < -C_{44}$. It is revealed that the operative direction of the AWP in this design can be tuned through the ratio C_{11}/C_{33} (Patil et al., 2019). As far as we know, the use of elastic anisotropy in the aforementioned cases inevitably introduces fundamental limitation in such a way that the polarization manipulation only functions along certain propagation directions (Zheng et al., 2019), which calls for the discovery of new solid media to dismiss the directional dependence.

Recently, the elastic polar solid was proposed as a perfect elastic wave cloaking material to have a generalized form-invariant constitutive behavior and possess elastic tensors with broken minor symmetry, making it an excellent candidates for elastic wave control devices (Nassar et al., 2018, 2019; Zhang et al., 2020; Nassar et al., 2020). As a matter of fact, the polar theory proposed can be seen as a version of micropolar elasticity simplified and modified to fit the requirements of the transformation method. The solid medium is polar in the sense that it elastically resists rotations and is also degenerate meaning it admits a stressless collapse mechanism. In the formulation, we neglect couple stresses but not body torque. Secondly, we assume that body torque is linearly dependent on deformations. Third, we embed torque equilibrium into Hooke's law. The outcome of this process is what we refer to as polar elasticity. Relaxing these constraints leads to a Cauchy medium. To implement the polar elasticity, anisotropic polar lattice materials were for the first time constructed by masses, hinge-like spring connection, and grounded torsional springs that resist rotations of the masses but free infinitesimal displacements (Nassar et al., 2018). The design enables an omnidirectional elastic cloaking and other static and dynamic field manipulation in both isotropic and anisotropic backgrounds. Later, 2D isotropic polar solids were developed as an isotropy-preserving transformation method to realize an elastic carpet cloaking (Nassar et al., 2019). Specifically, in the presence of isotropy, it is found that the elasticity tensor lacking minor symmetry features, in addition to the usual bulk and shear moduli, extra polarity and chirality moduli in 2D. The two new constants quantify to which degree stress and mirror symmetries are broken and provide additional degree for wave manipulation. The isotropic polar material admits the existence of a body torque density in order to induce non-symmetric stresses and wave polarization. To realize this property, we designed lattice-based materials to generate body torque distributions in the hexachiral lattice by leveraging grounded torsional springs (active approach) (Nassar et al., 2019; Xu et al., 2020) and/or internal rotating resonators (passive approach) (Nassar et al., 2020). The lattice-based sample for the active approach was fabricated using 3D printing in our previous experimental work (Xu et al., 2020). In that study, the polar material base is composed of two layers. One layer is to guide stresses and the other one is to impose the constraints to the nodes' rotations. For cloaking application, the polar material should also admit zero modes and degenerate, therefore, the polar material should be lattice-based materials so as to stretch or shear under zero stress.

In this study, the isotropic elastic polar media are leveraged to realize omnidirectional longitudinal-shear mode conversion and AWP by harnessing the polarity and chirality moduli. First, we briefly review the basic theory of the isotropic polar media. It is later found that polarity and chirality induced by the isotropy and non-vanishing asymmetric

stress with broken minor symmetries play an important role in achieving highly efficient mode conversion. Engineering the polar properties enables the isotropic polar medium to support the omnidirectional AWP which allows faster shear modes. This property subsequently leads to singly-polarized transmission and anomalous refraction. Unlike traditional schemes where elastic anisotropy is involved, all the polar media used are isotropic and allow the wave manipulation behaviors to operate in the absence of directional dependence. It is our hope that the proposed isotropic polar platform may provide additional insights into the development of modern elastic-wave-related devices.

1. Elastodynamics of 2D isotropic polar solids

1.1. Governing equations

We start with a brief review of a linear elastic polar solid governed by an equation of motion (Nassar et al., 2019)

$$\sigma_{ij,j} + \rho_p f_i = \rho_p \dot{v}_i, \quad (1)$$

where σ , ρ_p , f , and v denote the stress tensor, mass density, body force, and particle velocity, respectively. In general, strain energy $\psi(e)$ is dependent quadratically on the displacement gradient $e = u_{i,j}$, therefore, the general constitutive relation reads

$$\sigma_{ij} = \frac{\partial \psi(e)}{\partial e_{ij}} = a_{ijkl} e_{kl}, \quad (2)$$

where a should satisfy major symmetry $a_{ijkl} = a_{klij}$ but does not necessarily possess minor symmetries $a_{ijkl} \neq a_{ijlk}$. This means that the relation $\sigma_{kl} = \sigma_{lk}$ may not hold. The solid is "polar" with the existence of a body torque density linearly dependent over the displacement gradient as

$$c_i = \epsilon_{ijk} \sigma_{jk} = \epsilon_{ijk} a_{jklm} e_{lm}, \quad (3)$$

where c is the body torque and ϵ_{ijk} is the permutation symbol. In what follows, we will present a general expression of constitutive relations in 2D isotropic polar solid.

In 2D, a rotation angle θ is defined as the skew part of displacement gradient such that $\theta = \frac{1}{2}(u_{2,1} - u_{1,2}) = \frac{1}{2} \mathbf{J} : e$, where \mathbf{J} denotes the 2π rotation operation and $-J_{ij}$ is the 2D Levi-Civita notation. The deformation energy now reads

$$\psi = \mu \bar{e} : \bar{e} + \frac{1}{2} \kappa t^2 + \frac{1}{2} \alpha \theta^2 + \beta t \theta, \quad (4)$$

where $t = \text{tre}$, μ is a shear modulus transforming the deviatoric strain \bar{e} into the deviatoric stress $\bar{\sigma}$, κ and α conjugated to $\frac{\partial^2 \psi}{\partial t^2}$ and $\frac{\partial^2 \psi}{\partial \theta^2}$ respectively represent a bulk modulus and a polarity modulus. The former transforms the infinitesimal change of area t into a hydrostatic pressure p , while the latter transforms the infinitesimal rotation θ into a body torque c and breaks the minor symmetry, β is induced by the minor symmetry breaking and isotropy and represents the coupling between θ and t . With this decomposition, the strain-stress relation in terms of deviatoric, hydrostatic, and skew stresses can be expressed as,

$$\bar{\sigma} = 2\mu \bar{e}, \quad p = -\kappa t - \beta \theta \quad \text{and} \quad c = -\beta t - \alpha \theta, \quad (5)$$

which are illustrated in Fig. 1. In other words, hydrostatic pressure and body torque are coupled. Therein, the elastic tensor specifies into

$$a_{ijkl} = \mu(\delta_{ik}\delta_{jl} + \delta_{il}\delta_{jk}) + (\kappa - \mu)\delta_{ij}\delta_{kl} + \frac{\alpha}{4} J_{ij} J_{kl} + \frac{\beta}{2}(\delta_{ij} J_{kl} + J_{ij} \delta_{kl}), \quad (6)$$

and Hooke's law becomes accordingly

$$\sigma = (\kappa t + \beta \theta) \mathbf{I} + 2\mu \bar{e} + \frac{\beta t + \alpha \theta}{2} \mathbf{J}. \quad (7)$$

The isotropic polar solid addressed here corresponds basically to an extension of standard Cauchy elasticity with chiral and polar effects (Nassar et al., 2019). In order to enforce stability, μ , κ , α and β in Eq. (4) should remain positive (Nassar et al., 2019). Moreover, rewriting

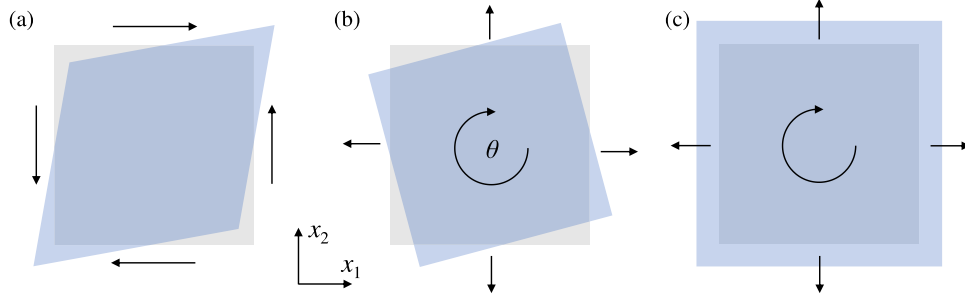


Fig. 1. Isotropic polar solids: response under (a) a pure shear, (b) a rigid rotation, and (c) a pure dilation.

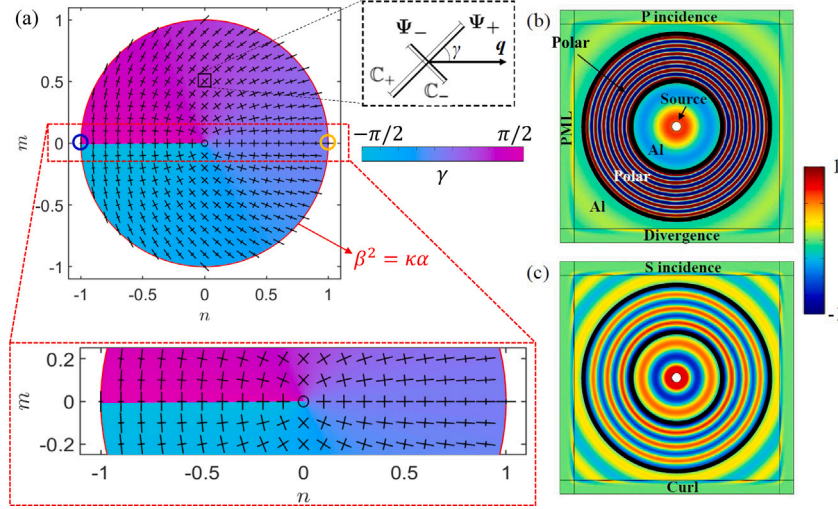


Fig. 2. (a) Polarization field in the m, n -space. The red circle corresponding to degenerate polar media bounds the stable region defined by the stability condition Eq. (8). The top inset is a magnified view of the polarization state and velocity magnitudes of Ψ_{\pm} at specific m and n . The bottom inset is another zoomed image for small m . The color map illustrates the m, n -dependence of polarization angle $\gamma = \arccos \sin \gamma_{+}$ of the faster mode Ψ_{+} . The blue and yellow circles represent two extreme polarization states ($n = -1, m = 0$ and $n = 1, m = 0$, respectively). Also, the yellow circle denotes a Cauchy-elastic medium. (b-c) show (b) the normalized divergence fields under a cylindrical P-polarized incidence and (c) the normalized curl fields under a cylindrical S-polarized incidence at 53 kHz. The cylindrical sources are realized with a circular boundary load at the center. The black solid curves indicate the isotropic polar slab ($c_p < c_s$, c_p and c_s being the phase velocity of P and S modes, respectively) with $m = 0.001$, $n = -0.999$, $l = 1$, $Q = 0.1244$ and a polar layer thickness of $0.859\lambda^{(P)}$, where $\lambda^{(P)}$ is the wavelength of P mode in the background at 53 kHz. The simulation domain is surrounded by perfect matched layers (PMLs).

Eq. (5) into matrix form and enforcing the determinant of the stiffness matrix to be non-negative yields the stability condition reading

$$\beta^2 \leq \kappa\alpha. \quad (8)$$

In the extreme case of $\beta^2 = \kappa\alpha$, where no parameters are zero, the isotropic polar solid becomes degenerate, and admits a zero mode where the stress is zero with non-vanishing displacement gradient (Nassar et al., 2019).

1.2. Wave propagation in the polar medium

We consider harmonic wave propagation in a 2D isotropic polar medium as

$$\mathbf{u} = \Psi e^{i(\mathbf{q}\cdot\mathbf{r}-\omega t)} = (u_1, u_2)^T e^{i(\mathbf{q}\cdot\mathbf{r}-\omega t)}, \quad (9)$$

where $\mathbf{q}\cdot\mathbf{r} = q_1x_1 + q_2x_2$ with \mathbf{q} and \mathbf{r} being the wave vector and position, respectively, Ψ and ω are, respectively, the wave amplitude and angular frequency. T represents the matrix transpose. By substituting the above equation into Eq. (7), we obtain the following secular equations

$$\begin{bmatrix} (\mu + \kappa)q_1^2 - \beta q_1 q_2 + (\mu + \frac{\alpha}{4})q_2^2 & \frac{\beta}{2}(q_1^2 - q_2^2) + (\kappa - \frac{\alpha}{4})q_1 q_2 \\ \frac{\beta}{2}(q_1^2 - q_2^2) + (\kappa - \frac{\alpha}{4})q_1 q_2 & (\mu + \kappa)q_2^2 + \beta q_1 q_2 + (\mu + \frac{\alpha}{4})q_1^2 \end{bmatrix} \Psi = \omega^2 \rho_p \Psi, \quad (10)$$

where $q_1 = q \cos \theta$, $q_2 = q \sin \theta$, and θ represents the propagation angle of the considered harmonic wave. Based on Eq. (10) and applying

$\bar{Q} = \kappa + \alpha/4$, $\mu = l\bar{Q}$, $\kappa - \alpha/4 = n\bar{Q}$ and $\beta = m\bar{Q}$, we obtain the wave phase velocities for the two orthogonal propagating modes

$$\mathbb{C}_{\pm}^2 = \frac{\bar{Q}(2l + 1 \pm \sqrt{n^2 + m^2})}{2\rho_p}, \quad (11)$$

where the “+/-” sign corresponds to the faster/slower eigenmode. In particular, μ , α , κ , and β in isotropic polar solids are represented by another four independent variables m, n, l , and \bar{Q} . The stability condition given by Eq. (8) now becomes $m^2 + n^2 \leq 1$ with $m^2 + n^2 = 1$ corresponding to the degenerate polar media. Note that we assume that the isotropic polar media used for illustrating wave manipulation functions throughout the paper are realized based on the grounding mechanism (Nassar et al., 2019; Xu et al., 2020), which causes broadband operability of the material parameters m, n, l , and \bar{Q} in the continuum limit. The material parameters can be determined from the bottom-up micromechanics homogenization method by analytically formulating the unit cell strain energy under global deformation (Nassar et al., 2019).

Based on Eq. (10), the wave mode shapes can be determined easily as $\Psi_{\pm} = (\sin \gamma_{\pm}, \cos \gamma_{\pm})^T$, where polarization angle $\gamma_{\pm} = \arctan \frac{\pm m}{\sqrt{n^2 + m^2 \mp n}}$. Fig. 2(a) illustrates the m, n -dependence of the modal polarizations (crosses) and the polarization angle γ of the faster mode with \mathbb{C}_{+} (color map). Therein, n quantifies to which degree the minor symmetry is broken whereas, m measures the intensity of the induced chirality and the handedness. The cross in the plot denotes the polarization states of the orthogonal modes Ψ_{\pm} , with the lengths representing phase velocities \mathbb{C}_{\pm} . Due to the isotropy of the polar solids, a wave vector \mathbf{q}

pointing towards the right is considered without loss of generality. The stability condition in Eq. (8) defines all possible polarized modes; see the red circular boundary in Fig. 2(a). First observation reveals that $m \neq 0$ leads to the existence of quasi-longitudinal (qP) and quasi-shear (qS) modes. This enables mode conversion functions between longitudinal (P) and shear (S) modes, as will be discussed later. Starting at the yellow circle (a Cauchy-elastic medium) and traveling across the first and second quadrants, the faster mode Ψ_+ transitions from being purely longitudinal to being purely shear. In other words, when $|\gamma| > \pi/4$ or $n < 0$, qS modes propagate faster than qP modes. Specifically, S modes outspeeding P modes can be seen when $|\gamma| = \pi/2$ is guaranteed, i.e. $m \rightarrow 0$ and $n < 0$, which leads to the occurrence of the AWP.

To numerically demonstrate the AWP that features faster S mode propagation, we conduct simulations using COMSOL for wave propagation in an isotropic polar slab sandwiched by two isotropic elastic media [see Figs. 2(b) and 2(c)]. The background medium used throughout the paper is aluminum ($\rho_0 = 2700 \text{ kg/m}^3$, $\mu_0 = 25.94 \text{ GPa}$, and $\lambda_0 = 50.35 \text{ GPa}$). Without loss of generality, the isotropic polar medium is set to be degenerate with $n = -0.999$, $m = 0.001$, $l = 1$, and $\rho_p = 5\rho_0$, $Q = 0.1244$, where a normalized parameter is defined as $Q = Q/(2\mu_0 + \lambda_0)$. The stiffness tensor with the additional polar constants are implemented with the help of a series of weak formulations to override the default elastic settings. The numerical results of the normalized divergence and curl fields are plotted in Figs. 2(b) and 2(c) under cylindrical P- and S-polarized incidences at 53 kHz in the inner background elastic medium. The choice of this frequency is based on the consideration that the polar slab offers large transmission for both polarized incidences at this frequency; see also Figs. 8(a) and 8(b) in Appendix. However, even so, there still exists nonzero reflections at both interfaces due to the slight impedance mismatching ($Z_s/Z_+ = 0.4517$ and $Z_p/Z_- = 1.2627$), as can be seen from the Figs. 2(b) and 2(c). We emphasize that under a certain polarized incidence the polar slab only supports the mode of the same polarization because the chiral effect vanishes in these cases. That said, it is reasonable to directly compare the wavelength to examine the comparison of velocity for both modes, although interference patterns from the reflection exists in the polar slab. The comparison of wavelength between the polar slab and the background shows $\lambda_p/\lambda_- = 6.3443$ for the P mode and $\lambda_s/\lambda_+ = 2.2591$ for the S mode, where λ_p , λ_s , λ_+ and λ_- represent the wavelengths of the background longitudinal and shear modes, and the faster and slower modes in the polar medium, respectively. By comparing the wavelengths inside and outside the isotropic polar slab, we can readily observe that the wavelength of the S mode is larger than that of the P mode in the polar medium with a wavelength ratio of $\lambda_-/\lambda_+ = 1.4137$, which indicates the faster S mode exhibits a phase velocity 0.4137 times larger than that of the slower P mode. Furthermore, the simulation results also demonstrate the omnidirectional nature of this phenomenon, which is significantly different from the case where the phenomenon occurs only at certain propagation angles due to anisotropy (Patil et al., 2019; Ledbetter and Kriz, 1982; Schoenberg, 1983; Lee et al., 2017; Ahn et al., 2018; Helbig and Schoenberg, 1987).

2. Wave mode conversion in a finite isotropic polar slab

Different from the conventional approaches based on material anisotropy, we will study the feasibility of using an isotropic polar slab to achieve efficient wave mode conversion omnidirectionally. The mode conversion here takes place in the polar medium by harnessing the additional two parameters α and β .

2.1. Wave propagation from the isotropic Cauchy medium to polar medium

Recall that $\beta = m\bar{Q}$ corresponds to the measure of chirality and handedness. It couples the plane rotation angle and the change of area. With m being nonzero, the longitudinal dominant and shear dominant motions are coupled in isotropic polar media. When a certain polarized

incidence strikes the interface between a Cauchy and an isotropic polar media, components of other polarization will be generated. Consider a Cauchy-polar interface shown in Fig. 3(a). Without loss of generality, we send in a harmonic P-polarized normal incidence of unity amplitude $e^{i(q_P x - \omega t)}$, where $q_P = \omega\sqrt{\rho_0/(2\mu_0 + \lambda_0)}$ denotes the wave number of P mode. The version of S-polarized normal incidence can be derived in a similar fashion. By removing the term $e^{i\omega t}$, the displacement fields on the left side of the interface including the reflected wave components can be prescribed as

$$u^{(l)} = e^{iq_P x_1} + r_{PP} e^{-iq_P x_1} \quad \text{and} \quad v^{(l)} = r_{PS} e^{-iq_S x_1}, \quad (12)$$

where $q_S = \omega\sqrt{\rho_0/\mu_0}$ is the wave number of S mode, and r_{PP} and r_{PS} are the reflection coefficients of the reflected P and S components from the P-polarized incidence, respectively. The transmitted waves can be expressed as

$$u^{(r)} = t_{PqP} \sin \gamma_+ e^{iq_+ x_1} + t_{PqS} \sin \gamma_- e^{iq_- x_1}, \quad (13)$$

$$v^{(r)} = t_{PqP} \cos \gamma_+ e^{iq_+ x_1} + t_{PqS} \cos \gamma_- e^{iq_- x_1}, \quad (14)$$

where t_{PqP} and t_{PqS} denote the transmission coefficients of the transmitted qP and qS components, $q_+ = \omega/C_+$, and $q_- = \omega/C_-$. Note that we have assumed throughout the paper that the isotropic polar medium is an extension of the standard Cauchy elasticity with body torques. Therefore, the continuity conditions at 2D Cauchy and polar media interface only involve two displacement continuity conditions (perpendicular to and parallel with the interface), and two Cauchy stress continuity conditions (normal and shear stresses). Based on Eqs. (10)–(14), we can determine stress fields at the interface reading

$$\sigma_{11}^{(l)} = i(2\mu_0 + \lambda_0)q_P e^{iq_P x_1} - i(2\mu_0 + \lambda_0)q_P r_{PP} e^{-iq_P x_1},$$

$$\sigma_{21}^{(l)} = -i\mu_0 q_S r_{PS} e^{-iq_S x_1},$$

$$\sigma_{11}^{(r)} = i\omega\rho_p C_+ t_{PqP} \sin \gamma_+ e^{iq_+ x_1} + i\omega\rho_p C_- t_{PqS} \sin \gamma_- e^{iq_- x_1},$$

$$\sigma_{21}^{(r)} = i\omega\rho_p C_+ t_{PqP} \cos \gamma_+ e^{iq_+ x_1} + i\omega\rho_p C_- t_{PqS} \cos \gamma_- e^{iq_- x_1}.$$

Therein, the displacement ($u^{(l)} = u^{(r)}$ and $v^{(l)} = v^{(r)}$) and stress continuity conditions ($\sigma_{11}^{(l)} = \sigma_{11}^{(r)}$ and $\sigma_{21}^{(l)} = \sigma_{21}^{(r)}$) at the interface lead to

$$\begin{pmatrix} -1 & 0 & \sin \gamma_+ & \sin \gamma_- \\ 0 & -1 & \cos \gamma_+ & \cos \gamma_- \\ Z_P & 0 & Z_+ \sin \gamma_+ & Z_- \sin \gamma_- \\ 0 & Z_S & Z_+ \cos \gamma_+ & Z_- \cos \gamma_- \end{pmatrix} \begin{pmatrix} r_{PP} \\ r_{PS} \\ t_{PqP} \\ t_{PqS} \end{pmatrix} = \begin{pmatrix} 1 \\ 0 \\ Z_P \\ 0 \end{pmatrix}, \quad (15)$$

where

$$Z_P = \sqrt{\rho_0(2\mu_0 + \lambda_0)}, \quad Z_S = \sqrt{\rho_0\mu_0}, \quad Z_+ = \rho_p C_+, \quad \text{and} \quad Z_- = \rho_p C_-.$$

Based on Eq. (15), the amplitudes of the reflection coefficients can be obtained as

$$r_{PP} = \frac{N_1 c_- s_+ - N_2 c_+ s_-}{N_3 c_- s_+ - N_4 c_+ s_-}, \quad (16)$$

$$r_{PS} = \frac{2(Z_P Z_- - Z_P Z_+) c_- c_+}{N_3 c_- s_+ - N_4 c_+ s_-}, \quad (17)$$

where

$$s_+ = \sin \gamma_+, \quad s_- = \sin \gamma_-, \quad c_+ = \cos \gamma_+, \quad c_- = \cos \gamma_-,$$

and

$$N_1 = Z_P Z_S + Z_P Z_- - Z_S Z_+ - Z_+ Z_-,$$

$$N_2 = Z_P Z_S + Z_P Z_+ - Z_S Z_- - Z_+ Z_-,$$

$$N_3 = Z_P Z_S + Z_P Z_- + Z_S Z_+ + Z_+ Z_-,$$

$$N_4 = Z_P Z_S + Z_P Z_+ + Z_S Z_- + Z_+ Z_-.$$

The total reflection reads

$$R_P = |r_{PP}|^2 + \frac{Z_S}{Z_P} |r_{PS}|^2. \quad (18)$$

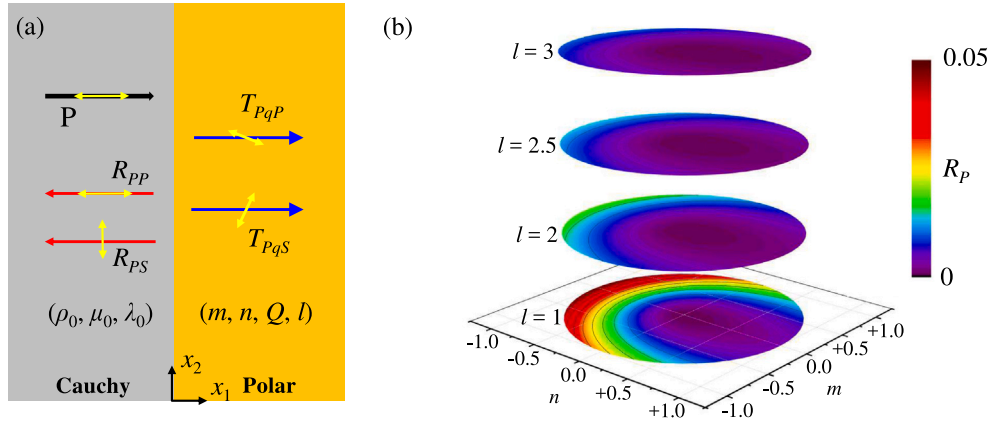


Fig. 3. (a) Schematic of an interface defined by a Cauchy (aluminum background) and an isotropic polar media. A P-polarized incidence and two types of reflections with r_{pp} and r_{ps} are within the aluminum background. The transmitted qP and qS modes with t_{pqP} and t_{pqS} exist in the polar region. The yellow arrows denote the polarizations. (b) Calculated reflectance R_p for the P-polarized incidence at the interfaces shown in (a) in functions of m and n , with $l = 1, 2, 2.5$ and 3 .

Eq. (18) can be further simplified as

$$R_p \approx \left(\frac{Z_+(Z_p - Z_s) + Z_p Z_s - Z_+^2}{Z_+(Z_p + Z_s) + Z_p Z_s + Z_+^2} \right)^2 \quad (19)$$

under the constraint of $Z_+ \approx Z_-$, which indicates that $(2l + 1)^2 \gg (m^2 + n^2)$ based on Eq. (11). This leads to the conclusion that $Z_+ \approx Z_p$ should be satisfied for achieving minimum reflection at the interface. Then, the optimal Q should be chosen as

$$Q = \frac{\rho_0}{\rho_p(l + 1/2 + \sqrt{m^2 + n^2})}, \quad (20)$$

as long as $(2l + 1)^2 \gg (m^2 + n^2)$ is well satisfied.

Without loss of generality, we consider $l = 1, 2, 2.5$ and 3 , and $\rho_p = 5\rho_0$. R_p at the interface is plotted in functions of m and n in Fig. 3(b). From 3(b), one can easily find R_p remains overall lower than 0.05 for all the (m, n) combination. As l increases, R_p continuously decreases, due to the approximation $(2l + 1)^2 \gg (m^2 + n^2)$, $Z_+ \approx Z_-$ being gradually bettered. In addition, a closer observation of Eq. (16) and (17) reveals that as $Z_+ \approx Z_p$ performs well, $|r_{ps}|$ almost vanishes, indicating that $|r_{pp}|$ dominates in the total reflection R_p .

2.2. Wave propagation in the polar slab between two isotropic Cauchy media

Here, we follow the discussion in the previous subsection and consider harmonic waves propagating in a finite isotropic polar slab of thickness L , sandwiched by two Cauchy media; see Fig. 4(a). A harmonic plane wave solution $\mathbf{u}_p = (u_1, u_2)^T$ in the sandwiched isotropic polar slab can be written as

$$\mathbf{u}_p = \begin{bmatrix} u_1 \\ u_2 \end{bmatrix} = \begin{bmatrix} \Psi_{+1}^{(+)} & \Psi_{+1}^{(-)} & \Psi_{-1}^{(+)} & \Psi_{-1}^{(-)} \\ \Psi_{+2}^{(+)} & \Psi_{+2}^{(-)} & \Psi_{-2}^{(+)} & \Psi_{-2}^{(-)} \end{bmatrix} \mathbf{P}_x^p \begin{bmatrix} A \\ B \\ C \\ D \end{bmatrix}. \quad (21)$$

Here, the superscripts “(+)” and “(-)” of both Ψ_+ and Ψ_- denote the propagation directions of $+x_1$ and $-x_1$, respectively. The subscripts “1” and “2” represent the first and second components of Ψ_{\pm} , respectively. A, B, C , and D are the displacement amplitudes, and $\mathbf{P}_x^p = \mathbf{I}(e^{iq_+x_1}, e^{-iq_+x_1}, e^{iq_-x_1}, e^{-iq_-x_1})^T$. For normal wave incidence, the field variables including the normal and shear stresses can be easily obtained at $x_1 = x$ as

$$\mathbf{F}_x^p = \begin{bmatrix} u_1 \\ u_2 \\ \sigma_{11} \\ \sigma_{12} \end{bmatrix} = \mathbf{Q}_p \mathbf{P}_x^p \begin{bmatrix} A \\ B \\ C \\ D \end{bmatrix}, \quad (22)$$

where \mathbf{Q}_p is given in Appendix. By linking the field variables at the two interfaces, i.e. $\mathbf{F}_L^p = \mathbf{T}\mathbf{F}_0^p$, we obtain the transfer matrix

$$\mathbf{T} = \mathbf{Q}_p \mathbf{P}_L^p \mathbf{Q}_0^{-1} (\mathbf{P}_0^p)^{-1}. \quad (23)$$

Similarly, the plane wave solution in the conventional isotropic media (μ_0, λ_0 and ρ_0) is written as

$$\mathbf{u}_s = A^s(1, 0)^T e^{iq_s^{(P)}x_1} + B^s(1, 0)^T e^{-iq_s^{(P)}x_1} + C^s(0, -1)^T e^{iq_s^{(S)}x_1} + D^s(0, 1)^T e^{-iq_s^{(S)}x_1}, \quad (24)$$

where the subscript “s” denotes the isotropic background, while the superscripts “(P)” and “(S)” correspond to P- and S-polarized incidences. Then, the field variables at $x_1 = x$ are

$$\mathbf{F}_x^s = \begin{bmatrix} u_1^s \\ u_2^s \\ \sigma_{11}^s \\ \sigma_{12}^s \end{bmatrix} = \mathbf{Q}_s \mathbf{P}_x^s \begin{bmatrix} A_x^s \\ B_x^s \\ C_x^s \\ D_x^s \end{bmatrix}, \quad (25)$$

where $\mathbf{P}_x^s = \mathbf{I}(e^{iq_s^{(P)}x}, e^{-iq_s^{(P)}x}, e^{iq_s^{(S)}x}, e^{-iq_s^{(S)}x})^T$, and \mathbf{Q}_s is given in Appendix. With the continuity conditions at interfaces $x_1 = 0$ and $x_1 = L$, stating $\mathbf{F}_0^s = \mathbf{F}_0^p$ and $\mathbf{F}_L^s = \mathbf{F}_L^p$, we have

$$\begin{bmatrix} A_L^s \\ B_L^s \\ C_L^s \\ D_L^s \end{bmatrix} = (\mathbf{P}_L^s)^{-1} \mathbf{Q}_s^{-1} \mathbf{T} \mathbf{Q}_0^s \mathbf{P}_0^s \begin{bmatrix} A_0^s \\ B_0^s \\ C_0^s \\ D_0^s \end{bmatrix} = \mathbf{S} \begin{bmatrix} A_0^s \\ B_0^s \\ C_0^s \\ D_0^s \end{bmatrix}. \quad (26)$$

The transmission and reflection coefficients of each polarization for the isotropic polar slab can be determined through \mathbf{S} . For instance, with a P-polarized incidence from the left, the scattering parameters, t_{pp} , t_{ps} , r_{pp} , and r_{ps} can be obtained simply from

$$\begin{bmatrix} t_{pp} \\ 0 \\ t_{ps} \\ 0 \end{bmatrix} = \mathbf{S} \begin{bmatrix} 1 \\ r_{pp} \\ 0 \\ r_{ps} \end{bmatrix}. \quad (27)$$

In the following, we will primarily concentrate on the P-to-S conversion. From Eq. (27) and Fig. 3(b), the conversion rate can be written by applying $r_{pp}, r_{ps} \approx 0$ as (Kweun et al., 2017)

$$T_{ps} = |t_{ps}|^2 \approx |S_{31}|^2 = D_s - E_s \cos(q_-L - q_+L) + G_s, \quad (28)$$

where

$$D_s = \frac{c_+^2 c_-^2}{2} \times \frac{Y^2(Z_s^2 Z_+^2 + Z_s^2 Z_-^2 + 2Z_+^2 Z_-^2) + X^2(Z_+^2 + Z_-^2 + 2Z_s^2) - 8XY Z_s Z_+ Z_-}{4Z_s^2 X^2},$$

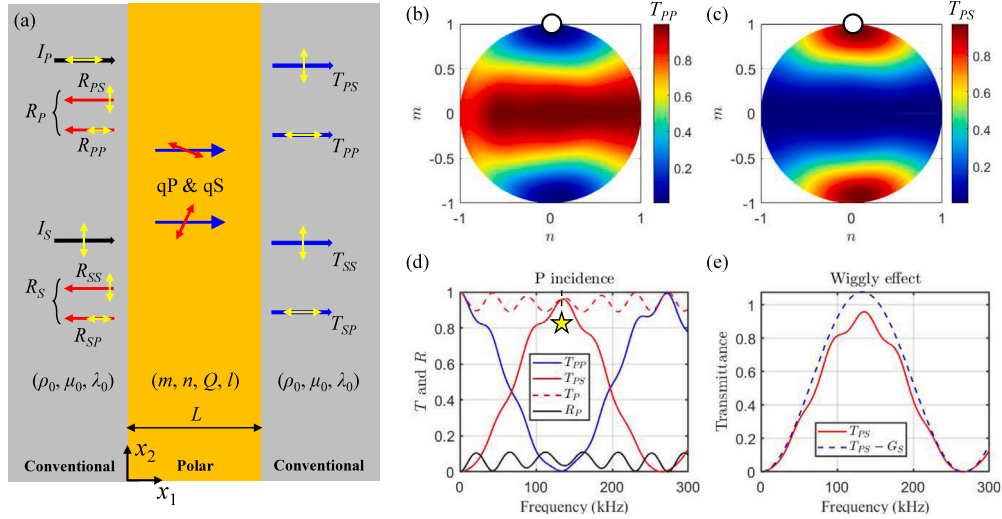


Fig. 4. Schematic of the sandwiched system defined by two Cauchy media and an isotropic polar slab. The incident wave I_p is indicated by a black solid arrow. All the scattered fields including the intermediate (blue), transmitted and reflected components are also identified. The yellow arrows for all the field components denote the polarization states. The thickness of the polar slab is L . (b–c) Calculated transmittance of (b) P-to-P and (c) P-to-S components of the sandwiched isotropic polar slab under P-polarized incidence in functions of m and n at $l = 1$. All results in (b–c) are calculated at $f = 144.1$ kHz with the aluminum background. The polar slab thickness is chosen as $L = 0.233\lambda^{(p)}$ at 144.1 kHz. A specific example related to the degenerate isotropic polar medium is taken at $m = 1$ and $n = 0$, and highlighted by the white circles. (d) Calculated frequency dependent scattering parameters of the isotropic polar slab under P-polarized incidence in the selected case in (b–c). The blue and red solid curves represent transmittance of P-to-P and P-to-S components, respectively. The red dashed and black solid curves correspond to the total transmittance and reflectance, respectively. The yellow pentagram indicates the first optimal mode conversion frequency. (e) Examination of the wiggly effect for P-polarized incidence.

$$E_s = \frac{c_+^2 c_-^2}{2} \times \frac{2Y^2(Z_s^2 Z_+ Z_- + Z_+^2 Z_-^2) + 2X^2(Z_+ Z_- + Z_s^2) - 2XY Z_s(Z_+ + Z_-)^2}{4Z_s^2 X^2},$$

$$G_s = \frac{B_s^2 - A_s^2}{2} \cos(2q_+ L) + \frac{B_s^2 - C_s^2}{2} \cos(2q_- L) - (B_s^2 + A_s C_s) \cos(q_- L + q_+ L),$$

with

$$X = \frac{\bar{Q}^2}{4} (m^2 + n^2 - 1 - 4l^2 - 4l),$$

$$Y = \frac{Z_p \sqrt{-X}}{\rho_p},$$

$$A_s = -\frac{Y Z_- c_+ c_-}{2X} + \frac{Z_+ c_+ c_-}{2Z_s},$$

$$B_s = -\frac{Y Z_+ Z_- c_+ c_-}{2Z_s X} + \frac{c_+ c_-}{2},$$

$$C_s = \frac{Y Z_+ c_+ c_-}{2X} - \frac{Z_- c_+ c_-}{2Z_s}.$$

Since G_s only introduces wiggly effect due to a non-vanishing structural instability, it does not necessarily influence the maximum conversion rate much as long as the reflection remains small (Kweun et al., 2017). Based on Eq. (28), the conversion rate is predicted to be a sine function of frequency owing to $q_{\pm} = \omega/C_{\pm}$, and the maximum conversion occurs at $(q_- - q_+)L = (2N - 1)\pi$, $N \in \mathbb{Z}$, where \mathbb{Z} denotes integer numbers. This condition corresponds to the transmodal Fabry–Perot resonance (Kweun et al., 2017) and implies that the optimal conversion frequency is inversely proportional to L . Then, the maximum conversion rate approximately takes the form of $T_{PS} \approx D_s + E_s$. Because $(2l + 1)^2 \gg (m^2 + n^2)$ when l takes large values, $2\sqrt{-X} \approx \bar{Q}(2l + 1)$ holds, leading to $D_s \approx E_s \geq 2c_+^2 c_-^2$. To optimize the conversion rate, one should aim to maximize $c_+^2 c_-^2 = m^2 / (4m^2 + 4n^2)$. This indicates that $n \rightarrow 0$ leads to the optimal conversion, while m mainly determines the occurrence frequency of optimal mode conversion. It is because $\beta = m\bar{Q}$ mainly induces the coupling between the shear and longitudinal motions. Note that the mode shapes Ψ_{\pm} at $n = 0$ ($\kappa = \alpha/4$) also

shows the optimal conversion always takes place when the polarization vectors of qP and qS modes are ± 45 degrees with respect to the propagation direction, namely $\gamma = \pi/4$.

Figs. 4(b) and 4(c) plot the m, n -dependence of wave transmittances T_{PP} and T_{PS} at 144.1 kHz. In the simulation, the parameters $\rho_p = 5\rho_0$ and $l = 1$ yielding sufficiently small reflection [Fig. 3(b)] are selected. It is found that the optimal conversion takes place around $n = 0$ and $m = 1$, which agrees well with the prediction. The conversion rate at this frequency is over 0.95 with vanishing transmission for unconverted P mode ($T_{PP} \rightarrow 0$). By selecting $m = 0.999$ and $n = 0.001$, we also plot the scattering spectra of the isotropic polar slab for P-polarized incidence in Fig. 4(d). The frequency dependence of T_{PP} (T_{PS}) follows roughly a cosine(sine) function, which is consistent with Eq. (28). The total reflectance R_p with magnitude overall lower than 0.1 exhibits oscillation over the frequency range due to Fabry–Perot resonances. At the optimal conversion frequency, $R_p = 0.03$ is achieved. Besides, Fig. 4(e) illustrates the influence of the wiggly term G_s , which primarily induces small perturbations on the transmittance curve as long as weak reflection is well achieved, and does not influence the frequency dependence. Note that, following the same procedure, one can obtain the expression of the same form as Eq. (28) for a S-polarized incidence, which suggests the same optimal conversion frequencies. However, the values of D_s , E_s and G_s will be generally different (Kweun et al., 2017).

To numerically verify the omnidirectional mode conversion, we utilize the simulation model used in Figs. 2(b) and 2(c) but with a different polar slab thickness. In particular, $l = 1$, $\rho_p = 5\rho_0$ and the same thickness L as that chosen in Fig. 4 are selected; see Fig. 5. At the center a cylindrical wave excitation of P wave is launched at the first optimal frequency, corresponding to the yellow pentagram in Fig. 4(d) [also see Figs. 5(a) and 5(b)]. At the optimal conversion frequency (144 kHz), the obtained divergence and curl fields of displacement indicate the occurrence of a nearly perfect omnidirectional mode conversion for P-polarized incidence. The reflection from the isotropic polar slab is heavily suppressed. In addition, we test the scattered fields for S-polarized incidence with the same configuration. As can be seen from Fig. 5(c) and 5(d), a highly efficient S-to-P conversion is also achieved

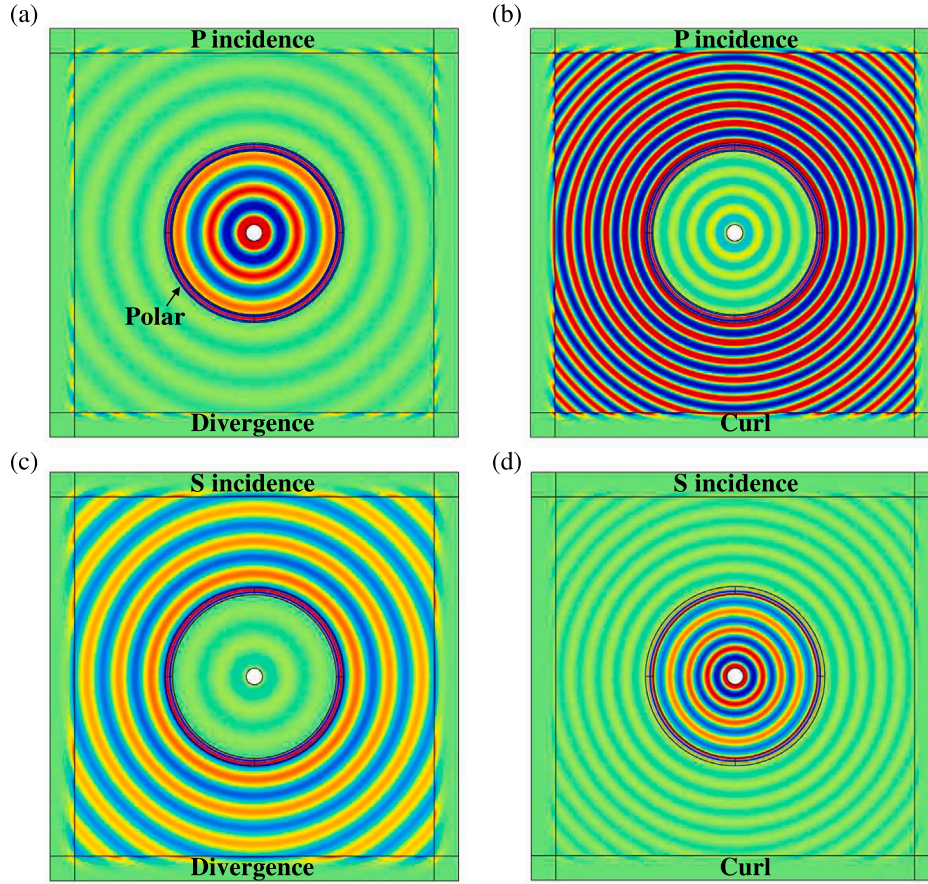


Fig. 5. Optimal omnidirectional mode conversion within a circular isotropic polar slab of a radial thickness $L = 0.233\lambda^{(P)}$ at 144.1 kHz. (a–b) show the normalized (a) divergence and (b) curl fields of displacement under the cylindrical P-polarized incidence. (c–d) give the normalized (c) divergence and (d) curl fields of displacement under the cylindrical S-polarized incidence. All the results are recorded at $f = 144.1$ kHz.

with minor reflection at the optimal conversion frequency, with an estimated conversion rate higher than 0.95.

3. Anomalous wave polarization in the polar medium

In addition to wave mode conversion, we point out that the polar media featuring the omnidirectional AWP can nearly perform as isotropic singly-polarized solids (SPS) where only S waves are allowed to be transmitted through omnidirectionally, without the necessity of elastic anisotropy (Zheng et al., 2019). Also, as a straightforward demonstration of the AWP, anomalous refraction is numerically realized that an oblique incidence of P wave produces zero transmitted S wave beyond a critical angle, when a P-polarized incidence propagates from a softer normal Cauchy to a harder isotropic polar media.

3.1. Omnidirectional quasi-singly-polarized transmission

As extreme cases, the isotropic polar media can be easily characterized as the singly polarized solids by properly harnessing the polar parameters. From Fig. 2(a), the existence of only P and/or S modes in the isotropic polar medium requires the chirality to be vanishing with $m \rightarrow 0$. Recalling the expressions of velocities given by Eq. (11), we find the smaller velocity C_- cannot reach zero because $l > 0$. However, an alternative way to approximate the singly-polarized solids is to find the case with $C_- \ll C_+$. By reexamining Fig. 2(a), the isotropic polar medium can be treated approximately as a singly-polarized solid supporting only P modes called longitudinal quasi-singly-polarized solid (QSPS) by taking $n \rightarrow 1$ and supporting only S modes called shear quasi-singly-polarized solid by taking $n \rightarrow -1$. Note that the latter

corresponds to an extreme case of the omnidirectional AWP where shear modes propagate faster. To numerically demonstrate these two QSPSs, we consider the term Q given by Eq. (20) without loss of generality. In order to meet the requirements for both longitudinal and shear QSPSs, we set $l = 0.001$ and $\rho_p = 0.5\rho_0$, which satisfy the stability condition. We select $m = 0.001$ and $n = \pm 0.999$ with “+” and “-” corresponding to a longitudinal and a shear QSPSs, respectively. The simulation model is exactly the same as the one illustrated in Fig. 5. Both S- and P-polarized incidences at 70 kHz are excited in the center. This frequency is chosen because it allows large transmission in the respective cases; see also Figs. 8(c) and 8(d) in Appendix. For the longitudinal QSPS, the P-polarized incidence is nearly fully transmitted through the polar slab, whereas the S-polarized incidence is mostly reflected by the polar slab to the inner background region, causing strong curl field intensities owing to the incidence and reflection superimposed; see Figs. 6(a) and 6(b). Note that the physical realization of this longitudinal QSPS with our previous grounded hexagonal lattices requires zero chirality and corresponds exactly to some existing architected materials such as “pentamode lattice”. In that type of lattices, the shear modulus nearly vanishes, causing longitudinal modes to drastically outspeed shear modes (Kadic et al., 2013, 2014). On the contrary, the shear QSPS forbids the transmission of P wave, but allows the transmission of S wave, as shown in Figs. 6(c) and 6(d). This agrees well with our previous analysis, and can be alternatively understood by impedance mismatching: the degrees of the impedance matching between the longitudinal QSPS and background aluminum for the P and S modes read $Z_+/Z_p = 1.2244$ and $Z_-/Z_s = 15.9303$, while for the shear QSPS, the two ratios become $Z_-/Z_p = 31.6254$ and $Z_+/Z_s = 0.6168$. Within the long-wavelength limit, the singly polarized

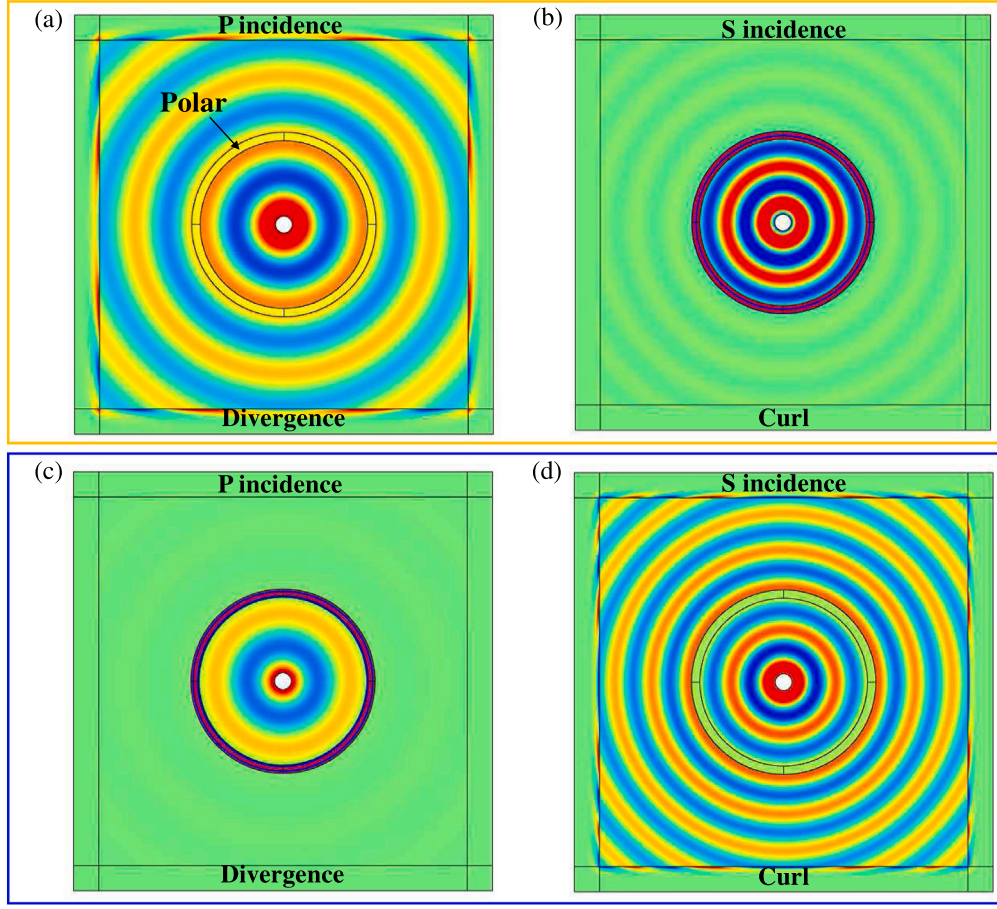


Fig. 6. Numerical demonstration of the omnidirectional singly polarized transmission at 70 kHz. The parameters of the polar media are chosen as $l = 0.001$, $\rho_p = 0.5\rho_0$, $m = 0.001$, $Q = 0.8$ and $L = 0.1134\lambda^{(p)}$ at 70 kHz, (a–b) $n = 0.999$ for a longitudinal QSPS, and (c–d) $n = -0.999$ for a shear QSPS. Normalized (a,c) divergence and (b,d) curl fields under P and S incidences for both the longitudinal and shear QSPSs are illustrated, respectively.

transmission is in general broadband except for several Fabry–Perot resonance frequencies (Nassar et al., 2019; Xu et al., 2020). Most importantly, the singly polarized transmission phenomenon for both polarized incidences occurs omnidirectionally, vastly differing from the anisotropic cases reported previously (Zheng et al., 2019).

3.2. Anomalous wave refraction

In general, when two isotropic media supporting only normal polarizations are separated by an interface, an oblique P-polarized incidence from the soft medium striking on the interface always generates both P- and S-polarized transmissions in the hard medium. This is simply because P modes possess larger phase velocities in these media, and will be converted into their S counterparts due to transverse phase matching. Here, we take advantage of the AWP from our isotropic polar media and demonstrate the anomalous refraction where beyond a critical angle, a P-polarized incidence will not yield any S-polarized transmission from a softer medium to a harder one. This originates from the fact that the faster mode becomes S-polarized with \mathbb{C}_+ when $m \rightarrow 0$ and $n < 0$, as has been indicated in the previous sections. According to Snell's law, the critical angle of incidence for the occurrence of the anomalous refraction is given by

$$\theta_c \approx \sqrt{\frac{2\rho_p}{\rho_0 Q(2l + 1 - n)}} \quad (29)$$

That said, a P-polarized incidence beyond θ_c from a conventional isotropic medium will not produce S-polarized refraction. For the corresponding numerical demonstration, we construct the isotropic

polar slab embedded in the isotropic Cauchy-elastic medium. The equi-frequency contours (EFCs) of the background and isotropic polar medium are presented in Fig. 7(a). A critical angle of 23.78° for the anomalous refraction can be obtained based on Eq. (29). Moreover, a critical angle for the P-polarized polarization is found to be 44.2° . In this case, we consider three angles of incidence for P-polarized incidence: 15° , 30° and 45° ; see Figs. 7(a). The corresponding simulations shown in Fig. 7(b–d) involve a Gaussian beam excitation. The isotropic polar region and the aluminum background are separated by an interface. In Fig. 7(b), apparently, for a small incidence angle ($15^\circ < \theta_c = 23.78^\circ$), both P- and S-polarized transmissions with finite amplitudes in the polar medium can be observed, and the propagation directions agree well with the EFC prediction. When the angle of incidence exceeds the critical angle for the anomalous refraction, i.e. $30^\circ > \theta_c$, the P-polarized incidence does not intersect with the EFC of the S mode in the polar medium [see Fig. 7(a)]. As a result, no S-polarized transmission exists in the polar area, as can be seen in Fig. 7(c). This is the direct numerical demonstration of the anomalous refraction for P-polarized incidence in our isotropic polar system. In addition, for a P-polarized incidence of 45° exceeding the critical angle for the P-polarized refraction (44.2°), neither P- nor S-polarized transmission can be observed in the polar region [see Fig. 7(d)].

Conclusions

In the study, the isotropic polar medium with extra polarity and chirality moduli is leveraged to realize complete mode conversion and anomalous wave polarization free from directional dependence. In

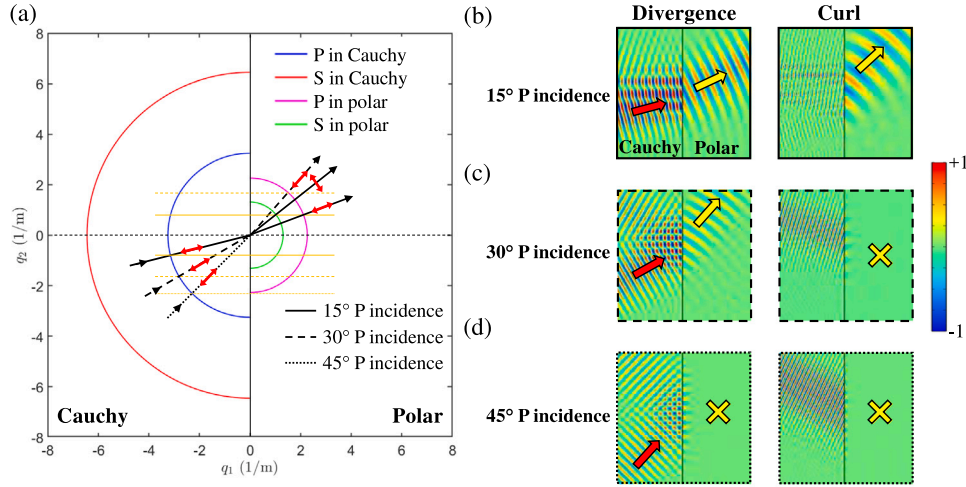


Fig. 7. Numerical demonstration of the anomalous refraction for P-polarized incidence. (a) EFC plots of the background aluminum and isotropic polar medium with $Q = 1.24$, $n = -0.999$, $l = 0.5$, and $\rho_p = 0.304\rho_0$ at angles of incidence of 15°, 30° and 45°. (b–d) show the normalized divergence and curl fields of displacement at 75 kHz under P-polarized incidence at angles of incidence (b) 15°, (c) 30° and (d) 45°. In the field illustrations, the red and yellow arrows stand for the incident and the calculated transmitted wave directions based on the EFC plot, respectively. The field intensities are normalized to the maximum amplitude. The yellow crosses indicate vanishing field amplitudes in the polar region.

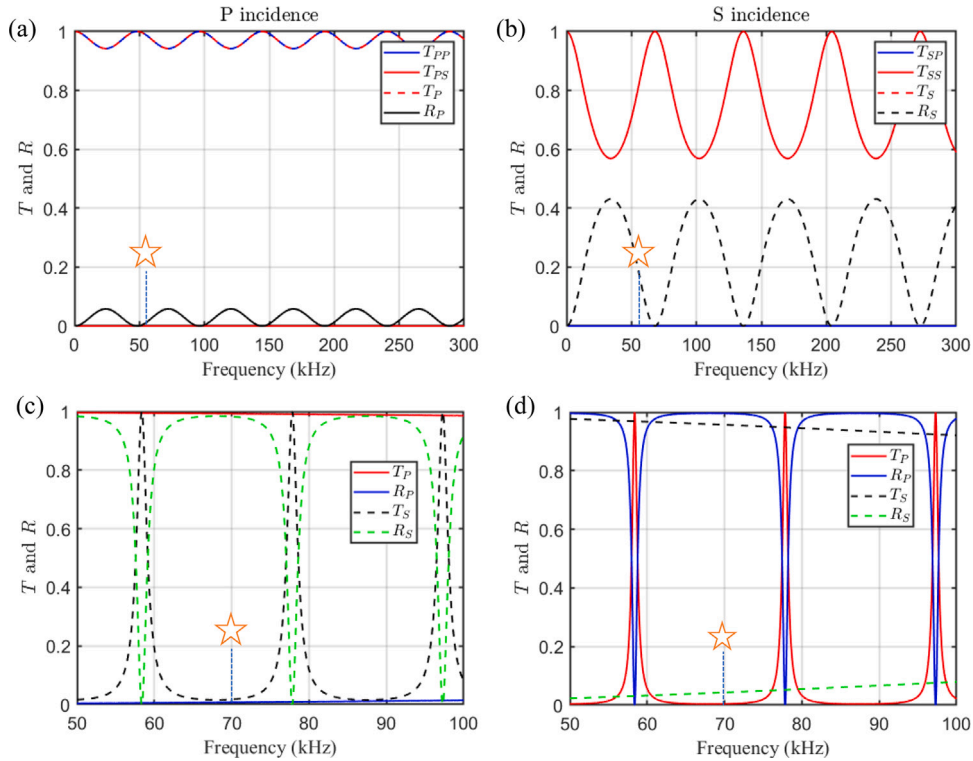


Fig. 8. (a,b) Frequency dependent transmission and reflection of (a) P incidence and (b) S incidence by the isotropic polar slab of $L = 100$ mm, $l = 1$, $Q = 0.1224$, $\rho_p = 5\rho_0$, $m = 0.001$, and $n = -0.999$. The marked frequency (53 kHz) is what we have used for the demonstration of the omnidirectional AWP that features faster shear mode in the main text. (c,d) Frequency dependent transmission and reflection by isotropic polar slabs of (c) $L = 10$ mm, $m = 0.001$, $n = 0.999$ and (d) $L = 10$ mm, $m = 0.001$, $n = -0.999$. The marked frequency (70 kHz) is what we have used for the demonstration of the omnidirectional singly polarized transmission in the main text. In all the figures, T and R represent the transmittance and reflectance, respectively. The subscripts “P” and “S” correspond to the P- and S-polarized waves, respectively.

the proposed isotropic polar system, non-vanishing asymmetric stress with broken minor symmetries plays an important role in delivering highly efficient omnidirectional mode conversion owing to the chirality. Nearly total wave mode conversion from longitudinal to shear waves or vice versa is analytically and numerically investigated through a finite polar slab by engineering the two polar parameters. The isotropic polar solid also enables omnidirectional anomalous wave

polarization which enables faster shear modes and leads to the omnidirectional singly-polarized transmission and anomalous refraction for longitudinal wave. The recent experimental realization of the elastic polar solids may push this research closer to practical applications (Xu et al., 2020). We believe the proposed wave manipulation schemes based on isotropic polar solids should be beneficial to the modern elastic mode conversion and wave steering devices.

CRedit authorship contribution statement

Qian Wu: Theoretical and numerical investigations, Discussed the result, Writing – original draft. **Guoliang Huang:** Design concept, Supervision, Discussed the result, Writing – original draft.

Declaration of competing interest

The authors declare that they have no known competing financial interests or personal relationships that could have appeared to influence the work reported in this paper.

Acknowledgment

This work is supported by the Army Research Office, USA under Grant No. W911NF-18-1-0031 with Program Manager Dr. Daniel Cole.

Appendix. Detailed expressions in transfer matrix method

The detailed expression of \mathbf{Q}_p in Eq. (22) is given below

$$\mathbf{Q}_p = \begin{bmatrix} \Psi_{+1}^{(+)} & \Psi_{+1}^{(-)} & \Psi_{-1}^{(+)} & \Psi_{-1}^{(-)} \\ \Psi_{+2}^{(+)} & \Psi_{+2}^{(-)} & \Psi_{-2}^{(+)} & \Psi_{-2}^{(-)} \\ Q31 & Q32 & Q33 & Q34 \\ Q41 & Q42 & Q43 & Q44 \end{bmatrix}$$

with

$$\begin{aligned} Q31 &= iq_+(a_{1111}\Psi_{+1}^{(+)} + a_{1121}\Psi_{+2}^{(+)} \\ Q32 &= -iq_+(a_{1111}\Psi_{+1}^{(-)} + a_{1121}\Psi_{+2}^{(-)}) \\ Q33 &= iq_-(a_{1111}\Psi_{-1}^{(+)} + a_{1121}\Psi_{-2}^{(+)} \\ Q34 &= -iq_-(a_{1111}\Psi_{-1}^{(-)} + a_{1121}\Psi_{-2}^{(-)}) \\ Q41 &= iq_+(a_{1211}\Psi_{+1}^{(+)} + a_{1221}\Psi_{+2}^{(+)} \\ Q42 &= -iq_+(a_{1211}\Psi_{+1}^{(-)} + a_{1221}\Psi_{+2}^{(-)}) \\ Q43 &= iq_-(a_{1211}\Psi_{-1}^{(+)} + a_{1221}\Psi_{-2}^{(+)} \\ Q44 &= -iq_-(a_{1211}\Psi_{-1}^{(-)} + a_{1221}\Psi_{-2}^{(-)}) \end{aligned}$$

The detailed expressions of \mathbf{Q}_s and \mathbf{P}_x^s in Eq. (25) is given below

$$\mathbf{Q}_s = \begin{bmatrix} c_s^{(P)} & c_s^{(P)} & s_s^{(S)} & s_s^{(S)} \\ s_s^{(P)} & -s_s^{(P)} & -c_s^{(S)} & c_s^{(S)} \\ Q31s & Q32s & 0 & 0 \\ 0 & 0 & Q43s & Q44s \end{bmatrix}$$

$$\mathbf{P}_x^s = \begin{bmatrix} e^{iq_s^{(P)}x} & 0 & 0 & 0 \\ 0 & e^{-iq_s^{(P)}x} & 0 & 0 \\ 0 & 0 & e^{iq_s^{(S)}x} & 0 \\ 0 & 0 & 0 & e^{-iq_s^{(S)}x} \end{bmatrix}$$

where all the denoted entries read

$$\begin{aligned} Q31s &= iC_{11}q_s^{(P)} \\ Q32s &= -iC_{11}q_s^{(P)} \\ Q43s &= -i\frac{1}{2}C_{66}q_s^{(S)} \\ Q44s &= -i\frac{1}{2}C_{66}q_s^{(S)} \end{aligned}$$

where $C_{11} = 2\mu_0 + \lambda_0$ and $C_{66} = \mu_0$

References

- Ahn, B., Lee, H.J., Kim, Y.Y., 2018. Topology optimization of anisotropic metamaterials tracing the target EFC and field polarization. *Comput. Methods Appl. Mech. Eng.* 333, 176–196.
- Auld, B.A., 1973. *Acoustic Fields And Waves In Solids*.
- Clement, G.T., White, P.J., Hynynen, K., 2004. Enhanced ultrasound transmission through the human skull using shear mode conversion. *J. Acoust. Soc. Am.* 115 (3), 1356–1364.
- Helbig, K., Schoenberg, M., 1987. Anomalous polarization of elastic waves in transversely isotropic media. *J. Acoust. Soc. Am.* 81 (5), 1235–1245.
- Kadic, M., Bückmann, T., Schittny, R., Gumbsch, P., Wegener, M., 2014. Pentamode metamaterials with independently tailored bulk modulus and mass density. *Phys. Rev. A* 2 (5), 054007.
- Kadic, M., Bückmann, T., Schittny, R., Wegener, M., 2013. On anisotropic versions of three-dimensional pentamode metamaterials. *New J. Phys.* 15 (2), 023029.
- Kweun, J.M., Lee, H.J., Oh, J.H., Seung, H.M., Kim, Y.Y., 2017. Transmodal Fabry-pérot resonance: theory and realization with elastic metamaterials. *Phys. Rev. Lett.* 118 (20), 205901.
- Ledbetter, H., Kriz, R., 1982. Elastic-wave surfaces in solids. *Phys. Status Solidi (B)* 114 (2), 475–480.
- Lee, H.J., Lee, J.-R., Moon, S.H., Je, T.-J., Jeon, E.-c., Kim, K., Kim, Y.Y., 2017. Off-centered double-slit metamaterial for elastic wave polarization anomaly. *Sci. Rep.* 7 (1), 1–13.
- Nassar, H., Chen, Y., Huang, G., 2018. A degenerate polar lattice for cloaking in full two-dimensional elastodynamics and statics. *Proc. R. Soc. A* 474 (2219), 20180523.
- Nassar, H., Chen, Y., Huang, G., 2019. Isotropic polar solids for conformal transformation elasticity and cloaking. *J. Mech. Phys. Solids* 129, 229–243.
- Nassar, H., Chen, Y., Huang, G., 2020. Polar metamaterials: a new outlook on resonance for cloaking applications. *Phys. Rev. Lett.* 124 (8), 084301.
- Noguchi, Y., Yamada, T., Otomori, M., Izui, K., Nishiwaki, S., 2015. An acoustic metasurface design for wave motion conversion of longitudinal waves to transverse waves using topology optimization. *Appl. Phys. Lett.* 107 (22), 221909.
- Park, J., Lee, D., Rho, J., 2020. Recent advances in non-traditional elastic wave manipulation by macroscopic artificial structures. *Appl. Sci.* 10 (2), 547.
- Patil, G.U., Shedge, A.B., Matlack, K.H., 2019. 3D auxetic lattice materials for anomalous elastic wave polarization. *Appl. Phys. Lett.* 115 (9), 091902.
- Reid, D.R., Pashine, N., Bowen, A.S., Nagel, S.R., de Pablo, J.J., 2019. Ideal isotropic auxetic networks from random networks. *Soft Matter* 15 (40), 8084–8091.
- Reid, D.R., Pashine, N., Wozniak, J.M., Jaeger, H.M., Liu, A.J., Nagel, S.R., de Pablo, J.J., 2018. Auxetic metamaterials from disordered networks. *Proc. Natl. Acad. Sci.* 115 (7), E1384–E1390.
- Sayers, C., Tait, C., 1984. Ultrasonic properties of transducer backings. *Ultrasonics* 22 (2), 57–60.
- Schoenberg, M., 1983. Reflection of elastic waves from periodically stratified media with interfacial slip. *Geophys. Prospect.* 31 (2), 265–292.
- Tufail, Y., Yoshihiro, A., Pati, S., Li, M.M., Tyler, W.J., 2011. Ultrasonic neuromodulation by brain stimulation with transcranial ultrasound. *Nat. Protoc.* 6 (9), 1453–1470.
- White, P.J., Clement, G.T., Hynynen, K., 2006. Longitudinal and shear mode ultrasound propagation in human skull bone. *Ultrasound Med. Biol.* 32 (7), 1085–1096.
- Wu, Y., Lai, Y., Zhang, Z.-Q., 2011. Elastic metamaterials with simultaneously negative effective shear modulus and mass density. *Phys. Rev. Lett.* 107 (10), 105506.
- Xu, X., Wang, C., Shou, W., Du, Z., Chen, Y., Li, B., Matusik, W., Hussein, N., Huang, G., 2020. Physical realization of elastic cloaking with a polar material. *Phys. Rev. Lett.* 124 (11), 114301.
- Zhang, H., Chen, Y., Liu, X., Hu, G., 2020. An asymmetric elastic metamaterial model for elastic wave cloaking. *J. Mech. Phys. Solids* 135, 103796.
- Zheng, M., Liu, X., Chen, Y., Miao, H., Zhu, R., Hu, G., 2019. Theory and realization of nonresonant anisotropic singly polarized solids carrying only shear waves. *Phys. Rev. A* 12 (1), 014027.
- Zhu, R., Liu, X., Hu, G., Sun, C., Huang, G., 2014. Negative refraction of elastic waves at the deep-subwavelength scale in a single-phase metamaterial. *Nature Commun.* 5 (1), 1–8.